

# Electron Injection at High Mach Number Quasi-Perpendicular Shocks : Surfing and Drift Acceleration

T.Amano and M.Hoshino

*Department of Earth and Planetary Science, University of Tokyo, 7-3-1 Hongo, Bunkyo-ku,  
Tokyo 113-0033, Japan*

amano@eps.s.u-tokyo.ac.jp

## ABSTRACT

Electron injection process at high Mach number collisionless quasi-perpendicular shock waves is investigated by means of one-dimensional electromagnetic particle-in-cell simulations. We find that energetic electrons are generated through the following two steps: (1) electrons are accelerated nearly perpendicular to the local magnetic field by shock surfing acceleration at the leading edge of the shock transition region. (2) the preaccelerated electrons are further accelerated by shock drift acceleration. As a result, energetic electrons are preferentially reflected back to the upstream. Shock surfing acceleration provides sufficient energy required for the reflection. Therefore, it is important not only for the energization process by itself, but also for triggering the secondary acceleration process. We also present a theoretical model of the two-step acceleration mechanism based on the simulation results, which can predict the injection efficiency for subsequent diffusive shock acceleration process. We show that the injection efficiency obtained by the present model agrees well with the value obtained by *Chandra* X-ray observations of SN 1006. At typical supernova remnant shocks, energetic electrons injected by the present mechanism can self-generate upstream Alfvén waves, which scatter the energetic electrons themselves.

*Subject headings:* acceleration of particles — cosmic rays — plasmas — shock waves

## 1. INTRODUCTION

The origin of nonthermal emission observed from a variety of astrophysical objects is still a major unresolved issue of plasma astrophysics. These include supernova shocks, extragalactic radio sources and active galactic nuclei. Among them, shocks of supernova remnants

(SNRs) are believed to be the most probable acceleration site of Galactic cosmic rays. Much theoretical and observational work has been devoted to particle acceleration processes around shock waves. One of the most widely applied theory is diffusive shock acceleration (DSA) theory (e.g. Bell 1978a,b; Blandford & Ostriker 1978). It has been very successful in providing a natural explanation for the power law distributions of high energy particles observed in many astrophysical sources. This process utilizes Alfvén wave turbulence as the particle scatterers. Under the assumption of elastic collision between particles and waves, energetic particles scattering back and forth across the shock front gain a net momentum because of the converging velocity fields. The theory was extended to include the finite shock size and the self-consistent wave excitation and applied to the Earth’s bow shock in order to account for the diffuse ion component observed in the upstream (e.g. Eichler 1981; Lee 1982). While in situ observations of energetic ions associated with interplanetary shocks and planetary bow shocks can be well explained by the DSA theory (e.g. Scholer et al. 1980; Gosling et al. 1981), energetic electrons thought to be accelerated by DSA process are rarely observed (Shimada et al. 1999). On the other hand, there is no doubt about the existence of ultra-relativistic electrons which may be accelerated by DSA process at SNR shocks. We still have no clear consensus on what determines the electron acceleration efficiency. The physics of electron acceleration at collisionless shocks is poorly understood so far.

The well-known difficulty is that thermal electrons cannot be easily scattered by Alfvén waves because of their small gyroradii. Injection from thermal pool to mildly relativistic energy by some other mechanisms is required. Levinson (1992) has examined electron injection process at strictly parallel shocks. He considered the self-consistent excitation of the whistler waves with cosmic ray electrons by applying the standard quasi-linear theory. It was shown that the injection of low energy electrons by the self-generated whistlers may be possible when the Alfvén Mach number exceeds  $43/\sqrt{\beta_e}$ , where  $\beta_e$  is the ratio of thermal electron pressure to magnetic pressure. On the other hand, Papadopoulos (1988) has taken a different approach. He considered an electron energization process within the shock transition region by strong plasma microinstabilities. It is well known that the reflection of upstream ions plays a dominant role in the structure of quasi-perpendicular shocks (e.g. Leroy et al. 1982). The reflected ions streaming relative to the upstream plasma could excite various plasma instabilities in the so-called foot region. Papadopoulos (1988) argued that the relative drift velocity exceeds the electron thermal velocity at high Mach number shocks and leads to the excitation of the Buneman instability (Buneman 1958). The Buneman instability gives rise to very rapid electron heating. As a result, the interaction between incoming/reflected ions and the preheated electrons permits the excitation of the ion acoustic instability. Cargill & Papadopoulos (1988) demonstrated the idea of the electron energization process by using a hybrid simulation code where ions are treated as particles whereas

electrons are assumed to be a massless charge-neutralizing fluid. Shimada & Hoshino (2000) extended their studies to include the electron dynamics in the shock structure by using a particle-in-cell (PIC) code where both ions and electrons are treated as particles. They found that localized large amplitude electrostatic solitary waves (ESWs) are produced in the nonlinear stage of the Buneman instability. They also argued that the rapid electron heating and acceleration are involved with ESWs. Now, the acceleration mechanism associated with ESWs is considered as electron shock surfing/surfatron acceleration (SSA) process (Katsouleas & Dawson 1983).

SSA mechanism for ions has been extensively studied by many authors (e.g. Sagdeev 1966; Lee et al. 1996; Zank et al. 1996). The process utilizes the electrostatic shock potential which is caused by inertia difference between ions and electrons in the shock transition region. Ions having energy smaller than the shock potential are reflected by the shock front and begin to gyrate around the upstream magnetic field. During their gyromotion in the upstream, they are accelerated parallel to the shock surface by the motional electric field. If the spatial scale of the shock potential is small compared to the ion inertial length, multiple reflection can occur (Zank et al. 1996). In contrast to this, electrons cannot be reflected by the shock potential. The electric field directed to the downstream is required. Hoshino (2001) argued that ESWs can play the similar role to the shock potential in ion shock surfing acceleration, because ESWs are associated with phase space electron holes (positively charged structures). Electrons trapped in ESWs can be accelerated by the motional electric field. This acceleration mechanism is very efficient, so that mildly relativistic electrons are generated within the shock transition region on a very short time scale. The process has attracted a considerable attention and investigated in detail by many authors (e.g. Dieckmann et al. 2000a; McClements et al. 2001; Hoshino & Shimada 2002; Schmitz et al. 2002a,b), because it may provide a clue to the electron injection problem.

In situ observations of the Earth’s bow shock also evidence the existence of ESWs in the shock transition region and associated electron heating (e.g. Bale et al. 1998, 2002; Hull et al. 2006). Oka (2005) has recently carried out a detailed investigation of the well-resolved high Mach number Earth’s bow shock ( $M_A \simeq 14$ ) observed by the Geotail satellite. He showed a clear coincidence between nonthermal electrons and the appearance of the broad band electrostatic noise (BEN) which is considered to be a signature of ESWs, although a plausible acceleration mechanism remains unanswered.

Most of previous studies concerning electron energization processes by microinstabilities at high Mach number shocks are restricted to the case of strictly perpendicular shock. On the other hand, a number of PIC simulations of quasi-perpendicular supercritical shocks have been conducted for many decades (e.g. Forslund et al. 1984; Lembege & Savoini 1992).

However, the main applications of these studies were planetary bow shocks and interplanetary shocks in the heliosphere. Here we extend these studies to very high Mach number quasi-perpendicular shocks. We find that SSA produces suprathermal electrons in the transition region of quasi-perpendicular shocks. The electron energization via SSA occurs within a relatively narrow region at the leading edge of the shock transition region where strong electrostatic waves are observed as in the case of strictly perpendicular shocks. The difference is that the preaccelerated electrons are further accelerated by the so-called fast Fermi acceleration process which is proposed by Wu (1984) and Leroy & Mangeney (1984). They considered a particle motion in the de Hoffman-Teller frame (HTF) where the motional electric field vanishes. In that frame, a particle having sufficiently large energy is reflected by the shock which acts as a fast moving magnetic mirror. The mirror reflection is adiabatic process, provided that a particle gyroradius is much smaller than the shock thickness. Therefore, the energy of reflected particle is conserved in the HTF. Then, after the interaction with the shock, the particle momentum parallel to the magnetic field measured in the upstream frame is increased by  $\Delta p = 2mV_1/\cos\theta_{Bn}$ , where  $m$ ,  $V_1$  and  $\theta_{Bn}$  are respectively, particle mass, the upstream plasma bulk velocity and the shock angle. Since the momentum increase is proportional to the reciprocal of  $\cos\theta_{Bn}$ , the acceleration becomes extremely efficient at nearly perpendicular shocks. While the acceleration efficiency increases with increasing the shock angle, the number of reflected particle rapidly decreases, because the initial energy required for the reflection increases.

Later, Krauss-Varban & Wu (1989) has shown that the fast Fermi process in the HTF is equivalent to shock drift acceleration (SDA) in the normal incidence frame (NIF) where the upstream velocity is parallel to the shock normal. In the NIF, a particle gains its energy by drifting parallel to the upstream motional electric field direction. Note that Krauss-Varban & Wu (1989) called the acceleration mechanism as gradient drift acceleration and distinguished it from SDA. Since SDA was usually based on the approximation that a particle gyroradius is large compared to the shock width and a particle has multiple interaction with the shock front. In this paper, however, we will not discriminate the difference and simply call the acceleration mechanism as SDA, because the physical mechanism is the same (gradient drift provides the energy gain).

The process has been extensively studied in order to account for observed energetic electrons in the upstream of the Earth's bow shocks (e.g. Krauss-Varban et al. 1989; Vandas 1995). However, detailed parametric survey of Vandas (2001) has demonstrated quantitative discrepancies between the theoretical expectation and observations. He argued that the process should be modified by some other nonadiabatic processes such as pitch angle scattering in order to explain observations. In addition to this, the required energy for the reflection of thermal electrons at very high Mach number shocks is unrealistically high. This process by

itself cannot account for the observed nonthermal electrons at high Mach number shocks.

Previous studies did not consider the effect of microturbulence in the shock transition region, which we show plays an important role in the generation of energetic electrons. In fact, SSA is a highly efficient acceleration mechanism, so that the preaccelerated electrons gain sufficient energy required for the reflection process. As a result, the preaccelerated electrons are further accelerated via SDA. This two-step acceleration mechanism is important for providing a seed population for subsequent DSA process. In fact, we will show that the reflected electron energy is large enough to be accelerated by DSA process when the Mach number is typical of SNR shocks.

We propose a theoretical model of the two-step acceleration mechanism based on the simulation results. The present model well explains the observed injection efficiency and the energy density of cosmic ray electrons which were obtained by detailed analysis of *Chandra* X-ray observation of SN 1006 (Bamba et al. 2003). Moreover, the present model predicts the shock angle dependence of the injection efficiency. This dependence again agrees well with the shock angle constraint, which is required to account for the observation by the DSA theory (Bamba et al. 2003; Yamazaki et al. 2004).

## 2. SIMULATION

We study the dynamics of ions and electrons in the self-consistent shock structure by utilizing a one-dimensional electromagnetic PIC code where both ions and electrons are treated as particles. A high-speed plasma consisting of electrons and ions is injected from the left-hand boundary of a one-dimensional simulation system and travels toward the positive  $x$ . The plasma carries a uniform magnetic field  $B_x$  and  $B_z$ . At the right-hand boundary, the particles are specularly reflected. Then, a shock wave is formed and propagates in the negative  $x$  direction. The downstream bulk speed becomes zero on average in the simulation frame. Initially, there are 100 particles for each species in each computational cell. The grid size is comparable to Debye length and the simulation box consists of 51200 grids. The plasma parameters are as follows: The upstream plasma  $\beta_e = \beta_i = 0.08$  ( $\beta_j \equiv 8\pi n T_j / B^2$ ), where  $n$ ,  $T_j$ ,  $B$  are the density, temperature, and magnetic field strength, respectively. The ratio of the plasma frequency to the electron cyclotron frequency is  $\omega_{pe} / \Omega_{ce} = 20$ . In order to reduce the computational costs, the ratio of ion to electron mass  $m_i / m_e = 100$  is used. The upstream Alfvén speed becomes  $5 \times 10^{-3}c$ , where  $c$  is the light speed. We use the plasma injection four velocity of  $U_0 = 5 \times 10^{-2}c$ . The Alfvén Mach number of the resultant shock wave is  $M_A \simeq 15$  in the shock rest frame. Several runs with different shock angles are conducted with keeping the upstream magnetic field strength unchanged. In this section, we

mainly discuss the results of a run with  $\theta_{Bn} = 80^\circ$ .

Figure 1 shows an overall structure of the shock transition region at  $\omega_{pe}t = 12000$  (corresponding to  $\Omega_{ci}t = 5.5$ ). From the top panel, ion phase space diagram in  $(X, U_{ix})$ , electron phase space diagram in  $(X, U_{ez})$ ,  $(X, U_{ex})$  and  $(X, K_e)$ , the magnetic field  $B_z$  and the electric field  $E_x$ , respectively. The plasma four velocity is normalized to the injection velocity  $U_0$ . The electron kinetic energy  $K_e = (\gamma_e - 1)m_e c^2$  is normalized to the injection energy  $K_{e0} = (\gamma_0 - 1)m_e c^2$ , where  $\gamma_e$  and  $\gamma_0$  are the Lorentz factors of each particle and the injection velocity, respectively. The magnetic field and the electric field are normalized to the  $z$  component of upstream magnetic field  $B_{0z} = B_0 \sin \theta_{Bn}$  and the corresponding motional electric field  $E_{0y} = U_0 B_{0z} / \gamma_0 c$ , respectively. The spatial scale is given in units of the electron inertial length  $c/\omega_{pe}$  in the upstream. The color of the phase space diagrams represents the logarithm of particle count in each bin. Note that the vertical scale of the fourth panel (electron energy spectra) is also shown in a logarithmic scale.

The basic structure of the shock transition region is similar to those obtained by previous simulation studies of strictly perpendicular shocks (e.g. Shimada & Hoshino 2000; Hoshino & Shimada 2002; Schmitz et al. 2002a,b). We can find two distinct ion components, the incoming and the reflected ions. Strong electrostatic turbulence is observed at the leading edge of the shock transition region ( $280 \lesssim X \lesssim 290$ ), where the relative drift velocity between the incoming electrons and the reflected ions becomes maximum. These electrostatic waves are excited by the Buneman instability. Strong energization of the upstream electrons coincides with the turbulent electrostatic waves as in the case of strictly perpendicular shocks. The heating and acceleration of electrons due to the turbulence occur on a very fast time scale. If we look at the deeper inside the shock transition region, the pre-heated electrons trigger the ion acoustic instability and the associated heating of incoming ions is evident in the top panel. The maximum growth rate of the ion acoustic instability is  $\gtrsim 10\Omega_{ci}^{-1}$ , which we obtain by using the standard linear dispersion analysis. The growth rate is large enough for the instability to develop within the shock transition region. Electrons are slowly heated up by the ion acoustic waves and the adiabatic heating process.

In addition to these features, which are common to strictly perpendicular shocks, we can clearly find energetic electrons streaming away from the shock front along the magnetic field. These parallel escaping energetic electrons can be seen in the second panel, which represents the  $z$  component of electron four velocity. Note that the  $z$  component of velocity is almost parallel to the magnetic field. Figure 2 displays the distribution functions of electrons in  $(U_x, U_z)$  plane taken at four different locations around the shock transition region. Just before the shock front (a), energetic electrons are observed as a distinct beam component. The typical beam drift velocity parallel to the magnetic field is  $u_{\parallel}/U_0 \sim 15$ .

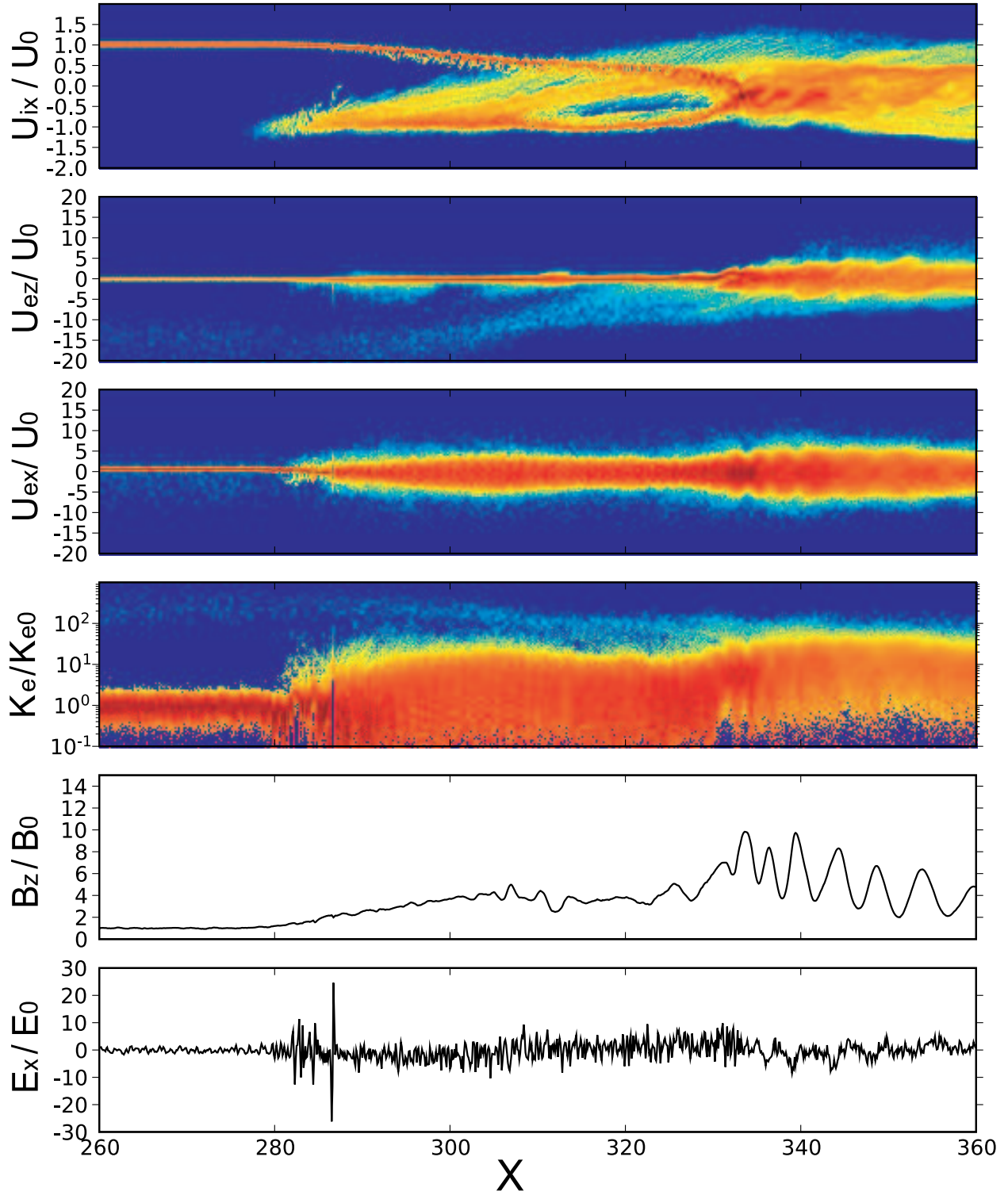


Fig. 1.— Overall shock structure of high Mach number quasi-perpendicular shock ( $\theta_{Bn} = 80^\circ$ ). Color represents the logarithm of particle count in each bin.

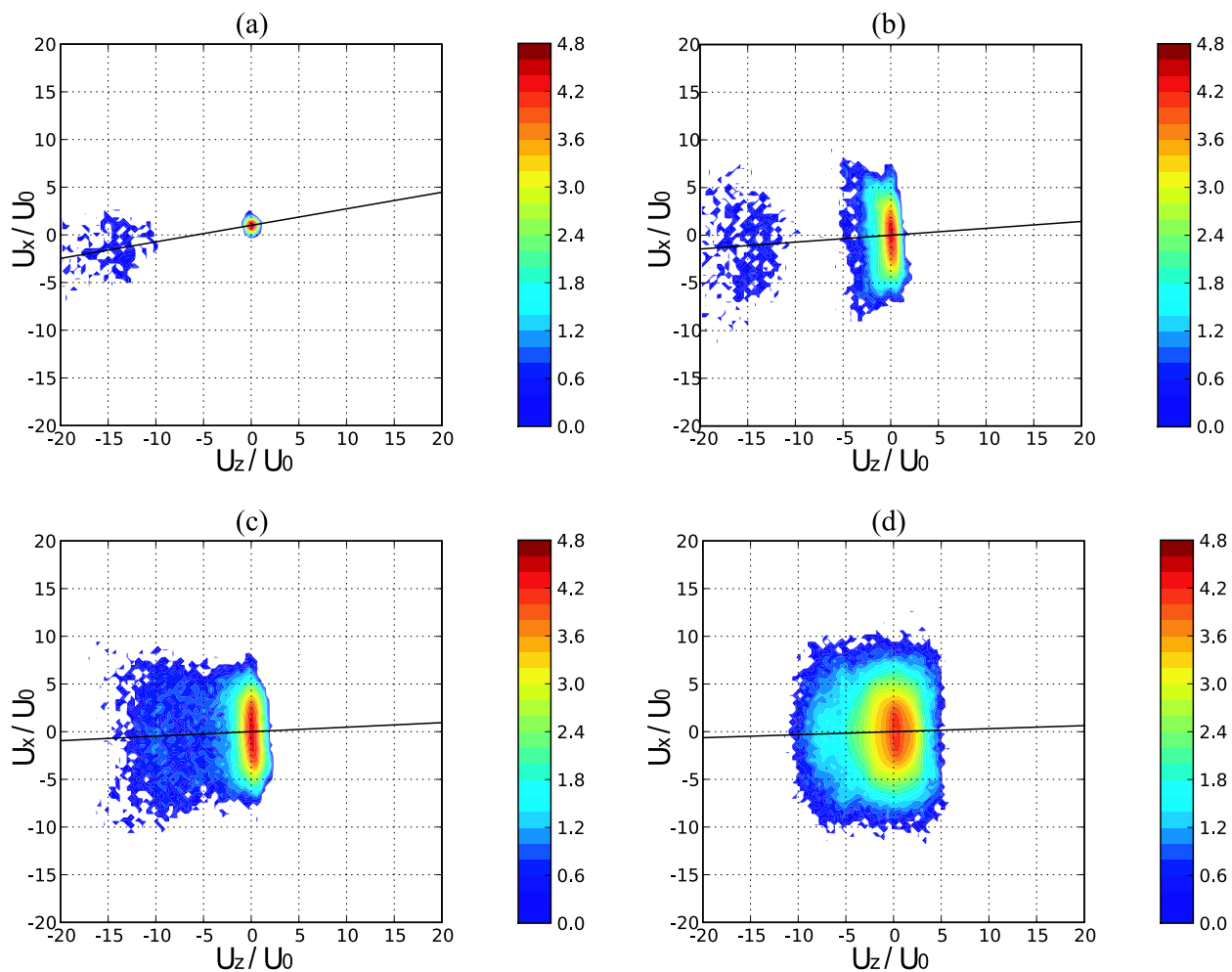


Fig. 2.— Distribution functions of electron in  $(U_x, U_z)$  plane. Each panel shows the distribution function taken at (a)  $260 < X < 280$ , (b)  $280 < X < 300$ , (c)  $300 < X < 320$ , (d)  $320 < X < 340$ , respectively. The solid line represents the direction of the averaged magnetic field. Color represents the logarithm of particle count in each bin.



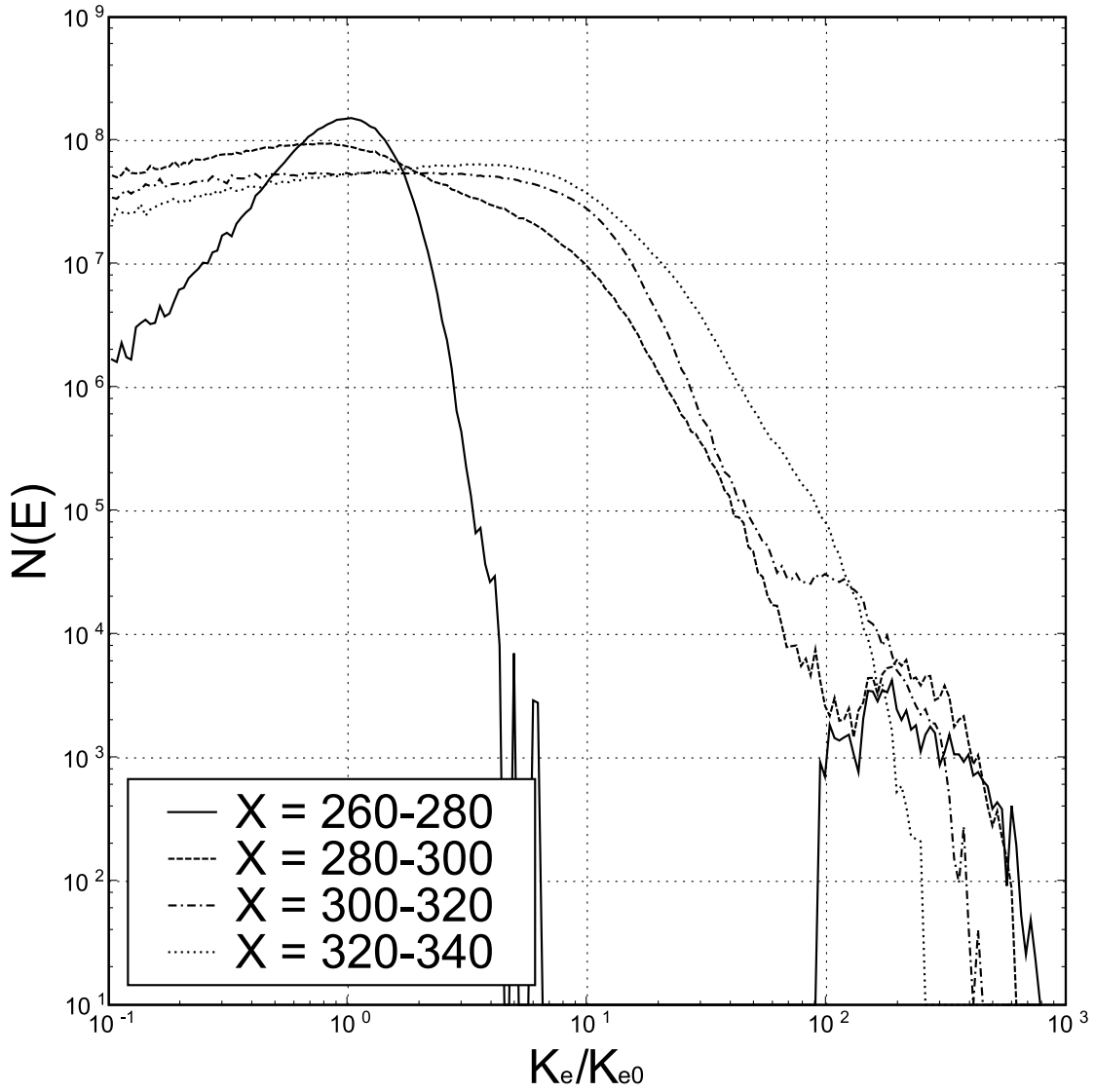


Fig. 3.— Energy spectra of electrons obtained around the shock transition region. Electron energy is normalized to the upstream bulk energy.

Since the electron beam excites Langmuir waves in the upstream, the cold upstream electron component is slightly modified from the far upstream condition. With increasing penetration into the shock, the incoming electrons are accelerated/heated up mainly perpendicular to the magnetic field, while the parallel drift velocity of the energetic electron beam decreases. Eventually, these two components merge into a single, but non-Maxwellian distribution (d). Figure 3 shows energy spectra of electrons. In the transition region ( $280 < X < 340$ ), the middle energy range ( $10 \lesssim K_e/K_{e0} \lesssim 100$ ) of the spectra can be approximated by the power law with indices of 3 – 4. On the other hand, humps are found in the high energy part ( $K_e/K_{e0} \gtrsim 100$ ) of the spectra. We observe the humps of the energy spectra only in the upstream or at the leading edge of the transition region ( $260 < X < 300$ ) but not in the downstream or the so-called overshoot region where the magnetic field strength is the largest. The fact indicates that the observed energetic electrons are the result of reflection (not the leakage of downstream particles). The reflected electrons are accelerated parallel to the magnetic field during the reflection.

In order to understand the electron acceleration process in more detail, individual trajectories of energetic electrons are analyzed. Figure 4 shows a trajectory of typical energetic electron. The left panel represents the trajectory of electron (thick line) with the stacked profiles of the magnetic field  $B_z$  (thin lines). The middle panel shows the time history of the particle energy. The solid, dotted and dashed lines of the panel display the perpendicular, parallel and total energy of the particle, respectively. The right-hand panel shows the time history of the first adiabatic invariant normalized to the upstream value. The unit of the vertical axis is the reciprocal of the electron gyrofrequency  $\Omega_{ce}^{-1}$ . The time history is plotted after  $\Omega_{ce}t = 300$  ( $\omega_{pet} = 6000$ ). As is evident from the stack plot of the magnetic field profiles, the shock front is highly nonstationary and periodically reforms itself with the characteristic time scale of  $\sim 2\Omega_{ci}^{-1}$ . The shock wave is propagating toward the negative  $x$  direction with the average speed of  $\sim 0.5U_0$ . Initially, the particle located in the upstream is convected toward the shock with the  $\mathbf{E} \times \mathbf{B}$  drift velocity. The particle first encounters the shock front at  $\Omega_{ce}t \sim 70$ , and gains quickly its energy within a short time of  $\Omega_{ce}\Delta t \sim 5$ . The energy of the particle increases by 2 orders of magnitude during the interval and the energy gain is almost perpendicular to the magnetic field. It is evident from the increase of the first adiabatic invariant that the process is highly nonadiabatic. This is indeed SSA mechanism investigated in detail by the previous studies (e.g. Hoshino & Shimada 2002). The properties of the acceleration are consistent with the previous results and we will not discuss the details of the process in any detail. After the first energization, the particle slowly drifts around the transition region without changing its energy until it collides with the overshoot at  $\Omega_{ce}t \sim 180$ . The particle is pushed toward the upstream direction by the magnetic mirror force during the collision and gains its total energy, whereas the first adia-

batic invariant remains almost constant. In other words, the particle is reflected by the shock acting as a fast moving magnetic mirror and gains its momentum parallel to the magnetic field. The parallel energy increases, while the perpendicular energy is almost constant or slightly decreases during the interaction.

The latter acceleration process associated with the reflection is known as SDA. As the shock angle and the upstream bulk flow speed increase, the energy gain of SDA increases. On the other hand, since the initial required energy for the reflection increases, the number of reflected particle rapidly decreases. Therefore, we expect that SDA process would not operate at high Mach number shocks. It is readily shown that the upstream thermal electrons of the present simulation cannot be reflected by the shock: The bulk velocities of the plasma in the upstream and downstream measured in the shock rest frame are  $U_1/U_0 \simeq 1.5$  and  $U_2/U_0 \simeq 0.5$ , respectively. The effective velocity of “the magnetic mirror” toward the upstream is  $U_s/U_0 = U_1/U_0 / \cos \theta_{Bn} \simeq 8.6$ . The loss cone angle denoted by  $\theta_c$  is given by

$$\sin \theta_c = \sqrt{\frac{B_1}{B_{max}}}, \quad (1)$$

where  $B_1$  and  $B_{max}$  are the magnetic field strength in the upstream and the overshoot, respectively. The reflection will take place when the condition  $u_{\perp} \gtrsim U_s \sin \theta_c$  is satisfied, where  $u_{\perp}$  denotes the perpendicular velocity of particle measured in the upstream frame. If we take a typical magnetic compression ratio of  $B_{max}/B_1 \simeq 10$ , the required velocity becomes  $U_s \sin \theta_c \simeq 2.7U_0$ . This condition is quite severe, because the upstream electron thermal velocity is only  $0.2U_0$ . Here, for simplicity, we ignore the effect of the electrostatic shock potential which suppresses the reflection efficiency. However, it cannot be neglected in general; hence, the reflection of thermal electrons requires even more stringent condition.

In contrast to the above theoretical analysis without any nonadiabatic process, our simulation results demonstrate the reflection does indeed take place, which we attribute to the presence of the preacceleration via SSA. Figure 5 shows a schematic illustration of the reflection process initiated by SSA process. The cold upstream electrons are energized by the electrostatic waves excited by the Buneman instability at the leading edge of the shock transition region. The energization is so efficient that a nonnegligible fraction of electrons escapes outside the loss cone on a time scale of  $\sim \Omega_{ce}^{-1}$ . The preaccelerated electrons escaping from the loss cone are subjected to SDA. In fact, by back tracing the trajectories of energetic electrons observed in the upstream side, we can confirm the scenario, i.e., the reflected electrons suffer the rapid energization via SSA when they enter the shock transition region and are reflected by the overshoot. On the other hand, low energy electrons are never reflected and just transmitted to the downstream. Therefore, we regard the two-step acceleration process as a preferential reflection process of energetic electrons. In the

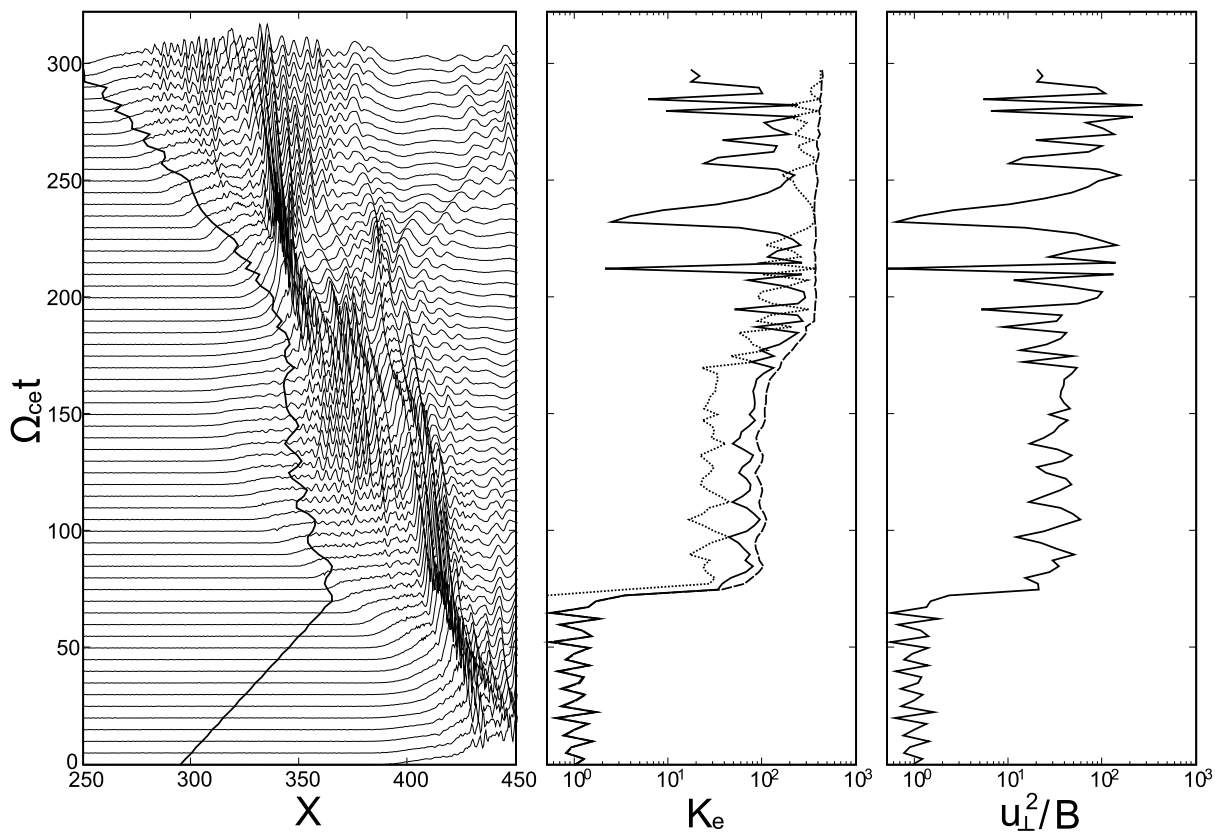


Fig. 4.— Time history of typical energetic particle. From left to right, particle trajectory (thick line) and stacked profiles of the magnetic field  $B_z$  (thin lines), particle energy, the first adiabatic invariant, respectively. The solid, dotted and dashed lines of the middle panel show the perpendicular, parallel and total particle energy, respectively. Energy and the first adiabatic invariant are normalized to the upstream values.

present mechanism, SSA plays a crucial role to trigger the secondary acceleration process. The important point is that SSA produces suprathermal particles with approximately the power law energy spectra. Since the shock potential considerably reduces the reflection efficiency, the expected heating due to the Buneman instability is not sufficient to provide the required reflection energy and the production of suprathermal particles is essential. It is also important that the acceleration is almost perpendicular to the magnetic field. Because of this, pitch angles of energetic electrons become large and they are easily reflected by the shock.

### 3. ELECTRON INJECTION MODEL

The reflection of energetic electrons discussed in the previous section can be considered as “electron injection” to subsequent DSA process. The reflected electrons observed as a beam component in the upstream drive several instabilities. It is well known that fast electron stream parallel to the magnetic field excites Langmuir waves via the bump-on-tail instability. We observe the enhanced Langmuir turbulence in the upstream of the simulation results, which is not seen in strictly perpendicular shocks. Energetic electrons streaming away from the shock and associated electrostatic turbulence are observed in the foreshock region of the Earth’s bow shock (e.g. Anderson 1969; Anderson et al. 1981; Kasaba et al. 2000). Another electromagnetic instability may also be excited by electron cyclotron resonance. We expect a left-hand polarized electromagnetic wave propagating parallel to the beam which can scatter the energetic electron themselves, provided that the beam speed is greater than  $\sim v_A \frac{m_i}{m_e}$ . As we will see in the discussion, this condition can be satisfied at shocks with Mach number typical of SNR shocks. Because of this, the initial field-aligned beam will tend to relax and become isotropic. From the above consideration, we recognize the reflected electrons as the seed population of DSA process, although a nonlinear evolution of the energetic electrons cannot be followed by our simulations because of the use of one-dimensional simulation box and a limited system size.

The density of reflected electrons is identical to the injection efficiency defined as  $n_e^{NT}/n_e$ , where  $n_e^{NT}$  is the number of nonthermal particles. Therefore, it is important to construct a theoretical model of the two-step acceleration process which predicts the injection efficiency and the energy density of nonthermal electrons relative to the thermal energy density.

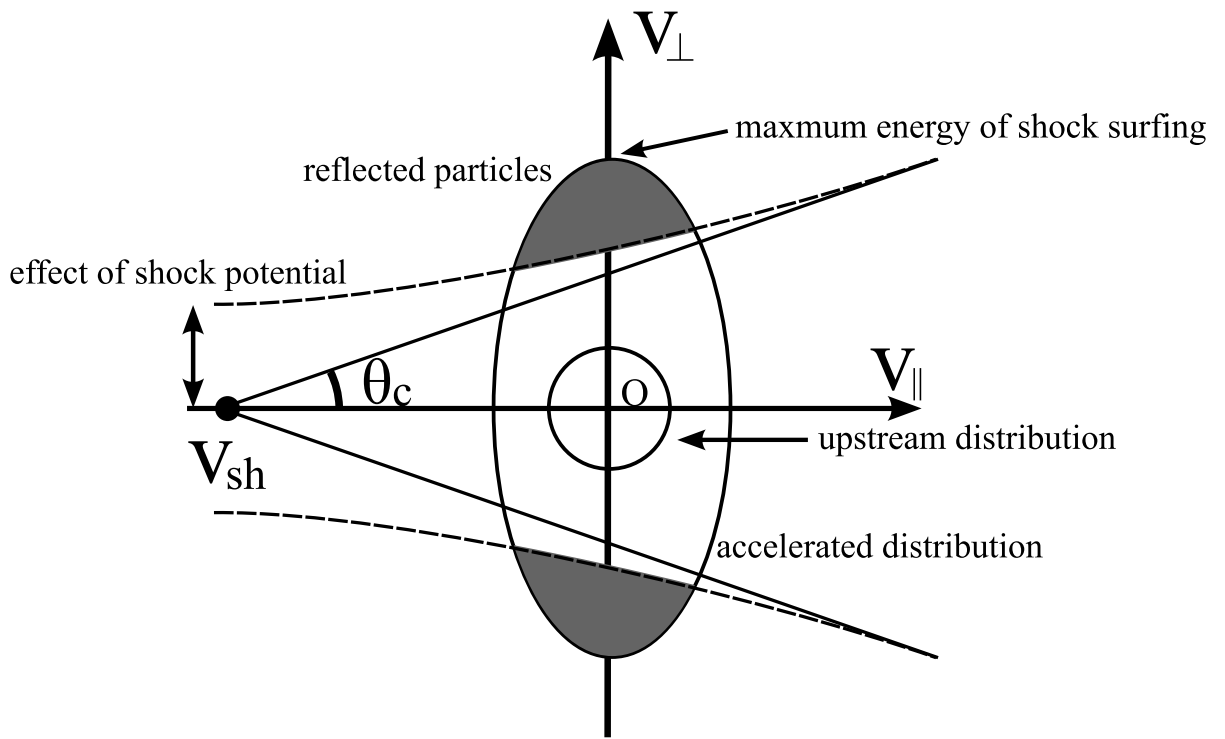


Fig. 5.— Schematic illustration of surfing and drift acceleration.

### 3.1. Electron Heating and Acceleration in the Foot

We investigate very high Mach number quasi-perpendicular shocks where the excitation of the Buneman instability is expected at the leading edge of the shock transition region. These shocks are typically observed around young SNRs. If we use the typical values of the magnetic field  $\sim 10\mu\text{G}$ , the density  $\sim 0.1\text{cm}^{-3}$  and the shock speed  $\sim 10^4\text{km/s}$  (e.g. Bamba et al. 2003), the Mach number of the shock becomes  $M_A = 100 - 1000$ . Although temperatures of upstream plasmas are difficult to estimate, they are probably very cold ( $\beta_e < 1$ ). Therefore, we can expect that the threshold condition of the Buneman instability

$$M_A \gtrsim \sqrt{\beta_e \frac{m_i}{m_e}} \quad (2)$$

is satisfied at these shocks.

In the following discussion, we neglect the relativistic effect for simplicity. However, we will show that the model agrees well with the simulation results which are in weakly relativistic regime (the maximum Lorentz factor of energetic electrons is  $\gamma_e \sim 2$ ).

Since the free energy of the Buneman instability is the relative streaming between the incoming electrons and the reflected ions, the amplitude of the electric field can be estimated as

$$\alpha \frac{1}{2} n_e m_e V_d^2 \simeq \frac{E^2}{8\pi}, \quad (3)$$

where  $\alpha$  is a energy conversion factor and  $V_d$  is the relative drift velocity (typically  $V_d \sim 2V_1$ ). Although the precise value of  $\alpha$  is hard to determine, it is a factor of the order of unity (Ishihara et al. 1981; Dieckmann et al. 2000b). We assume that the wave electric field is parallel to the shock normal as in the case of our one-dimensional simulations. Thus, the electric fields parallel and perpendicular to the upstream magnetic field are respectively given by  $E_{\parallel} = E \cos \theta_{Bn}$  and  $E_{\perp} = E \sin \theta_{Bn}$ , where  $\theta_{Bn}$  is the shock angle. By equating the electric field energy to the electron thermal energy in each direction (parallel and perpendicular), we estimate the resultant electron thermal velocity  $v_{e,\perp}$ ,  $v_{e,\parallel}$  after saturation as

$$v_{e,\perp} \simeq V_1 \sin \theta_{Bn} \quad (4)$$

$$v_{e,\parallel} \simeq V_1 \cos \theta_{Bn}, \quad (5)$$

respectively (Papadopoulos 1988).

In addition to the strong electron heating, the simulation results clearly demonstrate the formation of high energy tail in the electron energy spectra due to the Buneman instability.

Therefore, we employ the bi-kappa distribution (6) as a model distribution function in the foot,

$$f(v_{\parallel}, v_{\perp}) = \frac{n_f}{v_{e,\perp}^2 v_{e,\parallel}} \frac{\Gamma(\kappa + 1)}{(\pi\kappa)^{3/2} \Gamma(\kappa - 1/2)} \left[ 1 + \frac{1}{\kappa} \left( \frac{v_{\perp}^2}{v_{e,\perp}^2} + \frac{(v_{\parallel} - V_{sh})^2}{v_{e,\parallel}^2} \right) \right]^{-\kappa-1} \quad (6)$$

where  $\Gamma(x)$  is the gamma function,  $V_{sh}$  and  $n_f$  are the parallel drift velocity and the density in the foot, respectively. The distribution function is measured in the HTF. We define the foot as the region where the Buneman instability saturates. Hereafter, the subscript  $f$  represents the value in the foot. The incoming electrons are decelerated so as to cancel the zeroth order current, and somewhat compressed ( $n_f > n_1$ ). The mass conservation law leads to  $V_f = V_1 n_1 / n_f$ . The magnetic field is also compressed with the same compression ratio  $B_f = B_1 n_f / n_1$ . Thus, the parallel drift velocity of the compressed incoming electron is given by

$$V_{sh} = \frac{V_f}{\cos \theta_{Bfn}}, \quad (7)$$

which is almost equal to  $V_1 / \cos \theta_{Bn}$  for  $\theta_{Bn} \simeq 90^\circ$ . Here  $\theta_{Bfn}$  is defined as the angle between the shock normal and the magnetic field line in the foot.

### 3.2. Adiabatic Reflection

After the energization due to the Buneman instability, the ion acoustic instability is triggered and further electron heating may occur. However, this heating is not important for the generation of suprathermal electrons. Since we find that the first adiabatic invariant of energetic electron is conserved during the reflection process, we use the adiabatic approximation after the energization due to the Buneman instability. This approximation enables us to compute the reflected electron density by integrating the distribution function outside the loss cone. In general, the electrostatic shock potential is known to affect the mirror reflection process. If we include the finite potential measured in the HTF  $\phi^{HT}$ , the condition of the electron reflection becomes

$$v_{\perp}^2 \geq \left( v_{\parallel}^2 + \frac{2e}{m_e} \phi^{HT} \right) \tan^2 \theta_c \quad (8)$$

where  $\theta_c$  is the loss cone angle given by

$$\sin \theta_c = \sqrt{\frac{B_f}{B_{max}}}. \quad (9)$$



Here we use the foot to the maximum compression ratio to estimate the loss cone angle, because we use the adiabatic approximation after the energization in the foot. We consider  $B_{max}$  as the magnetic field strength in the overshoot. We know from both observations and numerical simulations that the shock potential is determined by the upstream bulk ion flow energy. Therefore, we normalize the shock potential to the bulk ion energy as

$$\tilde{\phi} = \frac{e\phi^{HT}}{\frac{1}{2}m_i V_1^2}. \quad (10)$$

The effect of the potential cannot be neglected when the particle parallel energy is comparable or smaller than the potential. Since the typical parallel velocity is expressed as  $v_{\parallel} \simeq V_{sh} \simeq V_1/\cos\theta_{Bn}$ , the condition can be written as

$$\tilde{\phi} \frac{m_i}{m_e} \cos^2 \theta_{Bn} \gtrsim 1. \quad (11)$$

For  $\tilde{\phi} = 0.4$  and  $m_i/m_e = 100$ , this condition leads to  $\theta_{Bn} \lesssim 81^\circ$ . Moreover, this critical angle increases with increasing  $m_i/m_e$ . The use of the realistic proton to electron mass ratio gives  $\theta_{Bn} \lesssim 88^\circ$ . Consequently, the effect of the shock potential is important for a wide range of shock angles and should be included in the injection model. We should note that the use of unrealistically small value of  $m_i/m_e$ , which is usual in most of PIC simulations, overestimates the reflection efficiency.

Although the shock potential in the HTF is identical to that in the NIF in the absence of the noncoplanar magnetic field component, significant field rotations out of the coplanarity plane within the shock transition region are often found by both in situ observations and numerical simulations (e.g. Thomsen et al. 1987). Our numerical simulations also produce the noncoplanar magnetic field component ( $B_y$ ) in the transition region. However, Krauss-Varban & Wu (1989) showed that the effect of the noncoplanar magnetic field component is only of second order in  $B_y/B$  and thus has little influence on the electron kinetics. Therefore, we can use the potential measured in the NIF as  $\phi^{HT}$ .

The reflected electron density  $n_r$  can be written as

$$n_r = 2\pi \int_0^\infty dv_{\parallel} \int_{\sqrt{v_{\parallel}^2 + \frac{2e}{m_e} \phi^{HT} \tan \theta_c}}^\infty v_{\perp} dv_{\perp} f(v_{\parallel}, v_{\perp}). \quad (12)$$

Evaluating the integral analytically, we obtain

$$n_r = \frac{n_f}{2v_{e,\parallel} r^\kappa \sqrt{\kappa\pi}} \left[ \sqrt{\frac{r}{p}} \pi - \frac{2q}{p} \frac{\Gamma(\kappa)}{\Gamma(\kappa - 1/2)} F\left(\frac{1}{2}, \kappa, \frac{3}{2}; -\frac{q^2}{rp}\right) \right], \quad (13)$$

where  $F(\alpha, \beta, \gamma; x)$  is the Gauss hypergeometric function and  $p$ ,  $q$ , and  $r$  are respectively given by

$$p = \frac{\tau + \tan^2 \theta_c}{\kappa v_{e,\perp}^2} \quad (14)$$

$$q = \frac{V_{sh}}{\kappa v_{e,\parallel}^2} \quad (15)$$

$$r = \frac{\frac{2e}{m_e} \phi^{HT} \tan^2 \theta_c}{\kappa v_{e,\perp}^2} + \frac{V_{sh}^2}{\kappa v_{e,\perp}^2} \frac{\tau \tan^2 \theta_c}{\tau + \tan^2 \theta_c} + 1, \quad (16)$$

using the anisotropy defined as  $\tau \equiv v_{e,\perp}^2/v_{e,\parallel}^2$ .

The reflected electron beam velocity measured in the shock frame can be easily estimated from the adiabatic theory as

$$v_r = V_{sh} \sqrt{\frac{B_{max} - B_f}{B_f - B_1}}. \quad (17)$$

The beam temperature can be determined by the integral

$$n_r T_r = 2\pi \int_0^\infty dv_{\parallel} \int_{\sqrt{v_{\parallel}^2 + \frac{2e}{m_e} \phi^{HT} \tan \theta_c}}^\infty v_{\perp} dv_{\perp} \frac{1}{2} m_e (v_{\parallel}^2 + v_{\perp}^2) f(v_{\parallel}, v_{\perp}). \quad (18)$$

However, we use a rather simple estimate instead of this. The thermal energy density of the reflected part of the distribution function can be written as

$$E_{th} = \int_{E_{min}}^\infty N(E) E dE = \int_{E_{min}}^\infty A E^{-k} dE, \quad (19)$$

where  $A$  and  $E_{min}$  are the normalization constant and the minimum energy required for the reflection, respectively. In the above integral, we approximate the energy spectrum by the power law part of the distribution function and the anisotropy is neglected. Substituting the normalization constant  $A = n_r \kappa E_{min}^\kappa$ , we obtain

$$E_{th} = n_r \frac{\kappa}{\kappa - 1} E_{min}. \quad (20)$$

The minimum energy is approximated by

$$E_{min} \simeq \left( \frac{1}{2} m_e V_{sh}^2 + e \phi^{HT} \right) \tan^2 \theta_c. \quad (21)$$

By combining these equations, we can write the energy density of the beam  $\epsilon_r$  as

$$\epsilon_r \simeq \frac{1}{2} n_r m_e v_r^2 + \frac{\kappa}{\kappa - 1} n_r \left( \frac{1}{2} m_e V_{sh}^2 + e \phi^{HT} \right) \tan^2 \theta_c. \quad (22)$$

This is somewhat crude estimate. Since the reflected beam distribution will be modified by nonadiabatic processes in the shock transition region, even the energy density estimated from the analytic integration (18) might be inaccurate. Nonetheless, (22) gives reasonably good estimate if it is compared to the simulation results. Therefore, we adopt this simple approximation. In the following discussion, density, velocity and energy will be given in units of the density, bulk velocity and bulk electron energy in the upstream, respectively. Note that, under this normalization, the result of the present model is independent of  $M_A$  and  $\beta_e$ , provided that (2) is satisfied.

### 3.3. Comparison Between Model and Simulation Results

Obviously, the injection efficiency strongly depends on the choice of  $\kappa$ . We adopt  $\kappa = 2.5$  (corresponding to the power law index of 3.5) which approximates the energy spectra in the shock transition region (see Figure 3). Likewise, the value of  $\tilde{\phi} = 0.4$  is used for the model calculation. The results depend weakly on the magnetic field in the foot and the overshoot. In the following discussion, we use the fixed values of  $B_f/B_1 = 2.5$  and  $B_{max}/B_1 = 10.0$  which are the typical values obtained from the simulation results. The variation of these values does not affect the result significantly.

Figure 6 shows the shock angle dependence of the density and the energy density of the reflected electrons calculated by the model with those obtained from the simulation results. The energy density of the model is converted to the downstream rest frame. The simulation results are averaged over  $X_{sh} - 70c/\omega_{pe} \leq x \leq X_{sh} - 20c/\omega_{pe}$ , where  $X_{sh}$  is the position at which the magnetic field is compressed by a factor of 1.5 from the upstream value. The time-averaged values during the last interval  $\Delta T \simeq \Omega_{ci}^{-1}$  of each run are shown. The error bars correspond to the variance during the interval.

The model curves agree well with the simulation results when the shock angle is small ( $\theta_{Bn} \lesssim 75^\circ$ ). However, the simulation results tend to deviate from the model curves with increasing the shock angle. At the shock angle of  $\theta_{Bn} = 85^\circ$ , no reflected electrons are observed in the simulation, while the model gives the density of  $\sim 4 \times 10^{-3}$ . This large difference is not acceptable when we apply the model to real shocks. In the next section, we introduce some modifications into the model in order to correct the discrepancy.

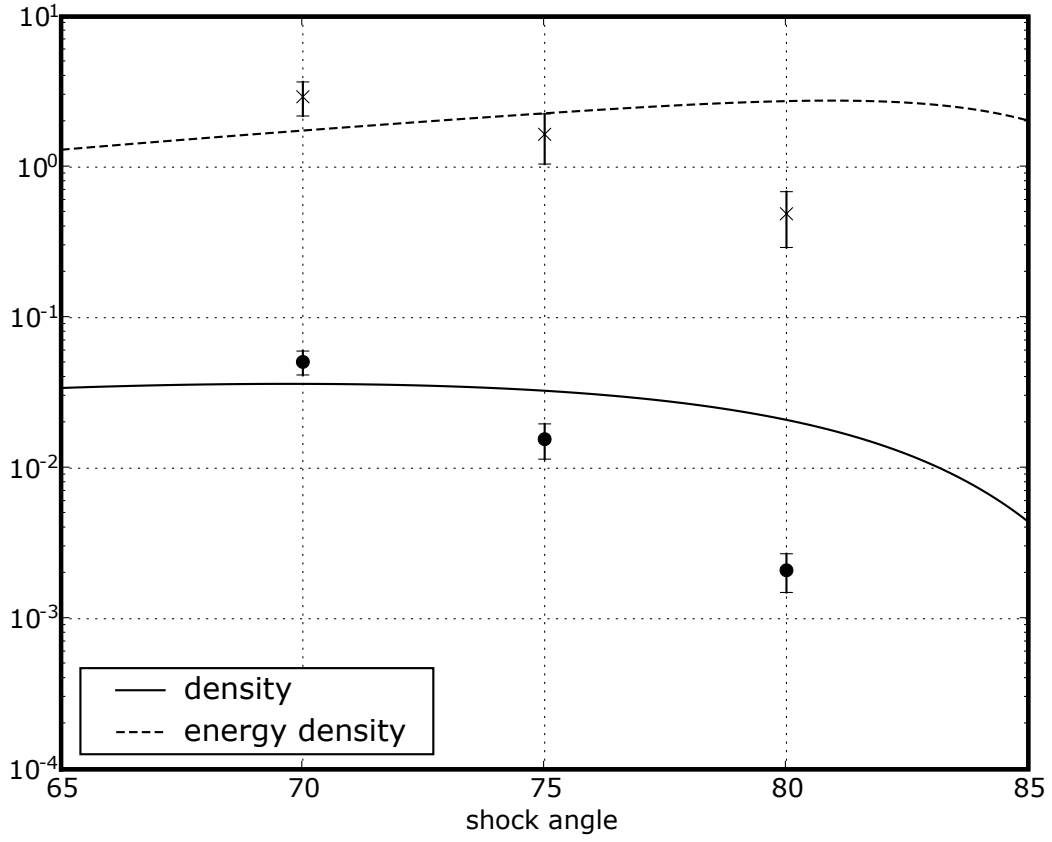


Fig. 6.— Comparison between our theoretical model and the simulation results. The solid and the dashed lines show density and energy density of reflected electrons calculated by the model. The simulation results are displayed by filled circles (density) and crosses (energy density).

### 3.4. Corrective Effects

#### 3.4.1. Maximum Energy Cut-Off of Shock Surfing Acceleration

The actual energy spectra obtained from the simulations have a cut-off energy where the number of particle rapidly falls off. Therefore, the number of reflected electron will fall off as  $\propto \exp(-E_{min}/E_{max})$ , where  $E_{max}$  is the maximum cut-off energy of SSA. It is easy to understand that the presence of the maximum cut-off energy becomes important when it is comparable or smaller than  $E_{min}$ . Because  $E_{min}$  increases with the shock angle, the presence of the maximum energy introduces the cut-off shock angle above which the reflection efficiency rapidly falls off. We can determine  $E_{max} \sim 100$  from the simulation results. This leads to the cut-off shock angle of  $\sim 86^\circ$ , which is larger than that of the simulation results.

Although only the above correction effect cannot explain why the reflected electron density of the simulation results show the rapid decrease at the shock angle  $\theta_{Bn} \gtrsim 80$ , the effect may be still important even when the shock angle is smaller than the cut-off, if we consider the application to real shocks. This is due to the fact that  $E_{min}$  strongly depends on the shock potential which increases with increasing the mass ratio. As discussed later,  $E_{max}$  should be larger than the shock potential in order to obtain a large fraction of reflected electrons.

#### 3.4.2. Escape Probability During Reflection

Although we use the adiabatic approximation after the first energization to compute the reflected electron density, the first adiabatic invariant may be violated in the presence of nonstationarity of the shock structure and/or the ion acoustic turbulence in the transition region. Particles which are initially outside the loss cone may be scattered by these effects and fall inside the loss cone. If we consider the escape probability  $P_{esc}$  as a constant both in time and space during the reflection, the number density will fall off as  $\propto \exp(-P_{esc}T_{ref})$ , where  $T_{ref}$  is the characteristic time for the reflection process. We can write  $T_{ref}$  by using initial perpendicular particle energy  $E_{ref}$  (see Appendix)

$$\Omega_{ci}T_{ref} \simeq \frac{2m_e V_{sh}^2}{E_{ref}/\tan^2 \theta_c - e\phi^{HT}}, \quad (23)$$

where the spatial gradient of the magnetic field strength and the electrostatic potential are assumed to be constant and the shock width is evaluated as  $V_1/\Omega_{ci}$ . We approximate the typical reflected electron energy before the reflection process as  $E_{ref} \simeq (E_{max} + E_{min})/2$ . It is readily shown that  $T_{ref}$  increases with increasing the shock angle, which leads to the

reduction of the reflection efficiency. We should note that the parameter  $P_{esc}$  is introduced as a free parameter to correct the discrepancy between the model and the simulation results. We determine the value of  $P_{esc}$  so that the model fits the simulation results.

Thereafter,  $P_{esc}$  will be given in the units of ion gyrofrequency  $\Omega_{ci}$ , because  $T_{ref}$  is of the order of ion gyroperiod.

### 3.4.3. Comparison Between Corrected Model and Simulation Results

Rewriting the density given by (13) as  $n'_r$ , above two effects can be included in the model with the following form

$$n_r = n'_r \exp\left(-\frac{E_{min}}{E_{max}} - P_{esc}T_{ref}\right). \quad (24)$$

Figure 7 shows a comparison between the simulation results and the model using the above correction. The format of the figure is the same as that of Figure 6. We use  $P_{esc} = 4$  and  $E_{max} = 100$  to produce the figure. In this case, we see that the model is significantly improved and the agreement becomes quite good. Therefore, we can conclude that the present model can predict the injection efficiency as well as the energy density of nonthermal particles, if the model parameters are properly estimated.

Note that the value  $P_{esc} = 4$  used here indicates that the underlying mechanism of electron scattering in the shock transition region is the self-reformation of the shock front, which occurs with the characteristic time scale of  $\sim 2\Omega_{ci}^{-1}$ . Since the shock structure considerably changes with this time scale, the motion of electrons interacting with the shock longer than this period may also be modified. As a result, only electrons which have sufficient energy for the rapid reflection can escape to the upstream.

## 3.5. Application to Supernova Shocks

Now, let us apply the model to SNR shocks. First, we should discuss the maximum energy of SSA. Since the shock potential is determined by the ion bulk flow energy, it will increase with increasing the mass ratio. The use of the same maximum energy  $E_{max}$  for the real mass ratio shock will result in the net reduction of the injection efficiency.

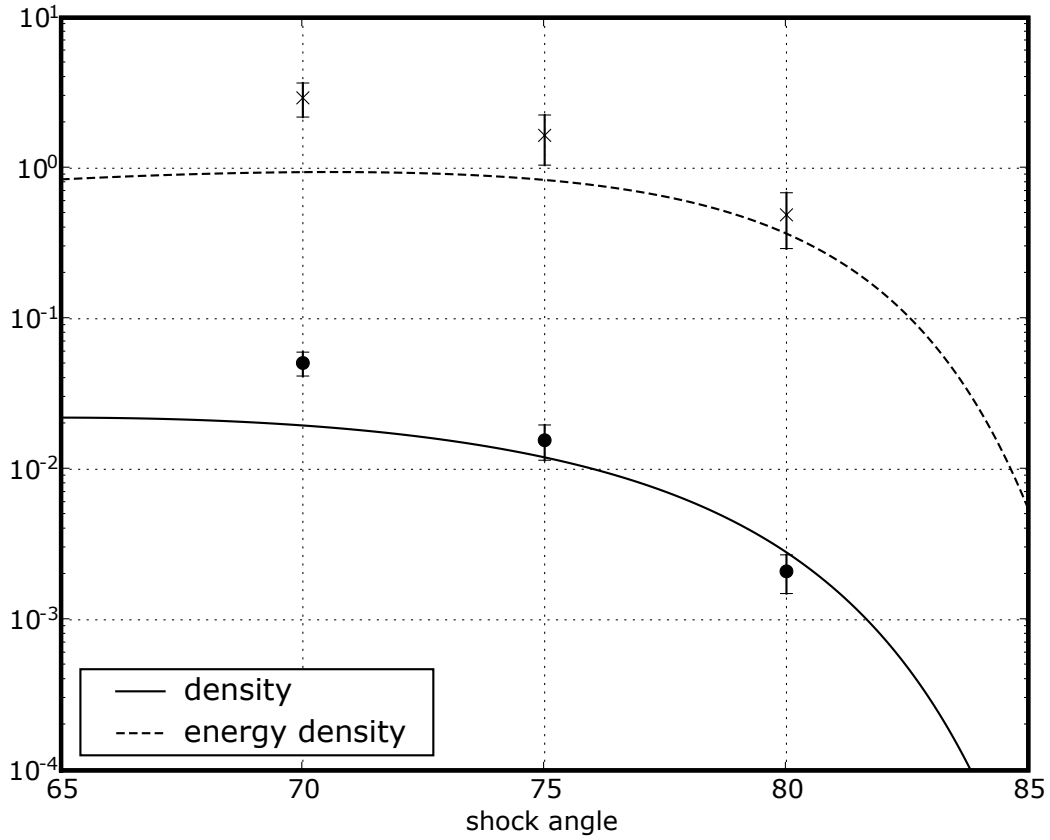


Fig. 7.— Comparison between our theoretical model with corrections and the simulation results. The format is the same as Figure 6.  $P_{esc} = 4$  and  $E_{max} = 100$  are used to produce the figure.

Hoshino & Shimada (2002) discussed the maximum energy of SSA and obtained the condition

$$2M_A \sqrt{\alpha \frac{m_e}{m_i}} \geq 1 \quad (25)$$

for “unlimited electron acceleration”, which means trapped electrons cannot escape from ESWs and continue to accelerate. They also mentioned that even in this regime, the trapping time might be limited by some other important factors. These include shock front nonstationarity (e.g. self-reformation) and multidimensional effects. In addition to this, the stability of ESWs is also a quite important factor limiting the trapping time. Dieckmann et al. (2000b, 2004) investigated the lifetime of the BGK mode excited by the Buneman instability using a periodic simulation model. They showed that the lifetime depends on the drift velocity of the reflected ions and also the background ion temperature. In our current understanding, it is still a hard task to estimate the trapping time scale. Furthermore, McClements et al. (2001) showed that stochastic electron acceleration can occur when  $\omega_{pe}/\Omega_{ce} \gg 1$ . In other words, electrons once detrapped from the potential can interact with the wave again. In this case, the maximum energy of SSA is not simply limited by the trapping time scale. It is very difficult to estimate the maximum energy of SSA and far beyond the scope of the present paper. We simply assume that the maximum energy increases with increasing the mass ratio from the following qualitative consideration: If the mass ratio is increased, the free energy provided by the reflected ions also increases. Since the free energy is the source of the energetic electrons, the maximum energy of SSA will also become higher.

If the maximum energy is smaller than the shock potential, the injection efficiency is greatly reduced independent of the shock angle. For typical values of the shock potential  $\tilde{\phi} \sim 0.4$ , we require  $E_{max} \gtrsim 750$  in order to obtain a measurable fraction of the reflected electrons. We assume  $E_{max} = 1000$  in the following discussion, which leads to the cut-off shock angle of  $\sim 88^\circ$ . In this case, the presence of the maximum energy cut-off does not significantly affect the result when the shock angle is smaller than the cut-off shock angle. Note that  $E_{max} = 1000$  corresponds to 10 – 100 keV at typical SNR shocks ( $V_1/c \sim 10^{-2}$ ).

The escape probability  $P_{esc}$  is also important in the sense that it introduces another cut-off shock angle. If  $P_{esc}$  is determined by the frequency of the self-reformation, it should be independent of the mass ratio. Therefore, we adopt  $P_{esc} = 4$  obtained by the simulation results of  $m_i/m_e = 100$ . This leads to the cut-off shock angle of  $\sim 85^\circ$ , which is smaller than that introduced by  $E_{max}$ . Namely, in the present parameter range,  $P_{esc}$  is more important than  $E_{max}$  for determining the shock angle dependence.

Figure 8 shows the injection efficiency (left) and the energy density (right) obtained by the present model. We consider the shock potential as a free parameter, because it is also



difficult to estimate the precise value of the shock potential at high Mach number shocks. We expect the potential will be in the range of  $\tilde{\phi} = 0.3 - 0.5$ . Then, we obtain the peak injection efficiency of  $\sim 2 \times 10^{-4}$  at  $\theta_{Bn} \simeq 80^\circ$ . Similarly, the energy density at the peak shock angle is approximately 10%.

These results can be directly compared to X-ray and radio observations of SNRs. Bamba et al. (2003) carried out a detailed investigation of the northeast shell of SN 1006 observed by *Chandra* and argued that the estimated injection efficiency is  $\sim 1 \times 10^{-3}$  and the energy density of nonthermal particles is about 30% of the thermal energy density. These values are similar to previous observations (e.g. Allen et al. 2001). The model prediction shows a good agreement with the observation, although the observed injection efficiency and the energy density of cosmic ray electrons are slightly larger than those obtained by the present model. Furthermore, the high resolution observation reveals that nonthermal emission is confined in very thin filaments. The spatial scales of the nonthermal filaments are  $\sim 0.04\text{pc}$  and  $\sim 0.2\text{pc}$  in the upstream and downstream, respectively. Similar results are also reported by Long et al. (2003). If the standard DSA theory is employed, the observed scale length of the nonthermal filaments imposes the constraint that the shock angle should be sufficiently large ( $\theta_{Bn} \gtrsim 80$ ), unless we assume the magnetic field of  $20 - 85\mu\text{G}$ , which is larger than the usual interstellar value of a few  $\mu\text{G}$  (e.g. Bamba et al. 2003; Yamazaki et al. 2004). The peak shock angle predicted by the model is around  $80^\circ$ , again we see a good agreement with the observation.

We should note that the peak shock angle depends on the choice of both  $P_{esc}$  and  $E_{max}$ . If  $E_{max}$  is sufficiently large compared to the shock potential, the peak shock angle is simply determined by  $P_{esc}$ . Although we attribute the escape probability to the shock front nonstationarity in the present analysis, there remain some other possibilities such as pitch angle scattering due to the interaction with the whistler waves in the shock transition region. The discussion of such nonadiabatic behaviors of energetic particles requires more detailed understandings of the structure and the wave activities in the shock transition region.

#### 4. DISCUSSION

We have studied rapid electron energization mechanism within the transition region of high Mach number quasi-perpendicular shocks. We found that highly energetic electrons are generated through successive two different acceleration processes. First, energetic electrons are produced via SSA at the leading edge of the shock transition region. As a result, the preaccelerated electrons escaping outside the loss cone are subjected to SDA and preferentially reflected back to the upstream. We consider the two-step acceleration mechanism as

the injection to subsequent DSA process. We have constructed a model of the acceleration mechanism which predicts the injection efficiency and the energy density of nonthermal particles. The estimated injection efficiency agrees well with observations of SN 1006. We also found that the shock angle dependence of the injection efficiency is consistent with the shock angle constraint inferred from observations.

Although the present model generally agrees well with observations, there remain some important issues. The most important one is the acceleration efficiency of SSA, i.e. the maximum energy and the spectral index. It is easily understood that the spectral index affect the injection efficiency to a great extent. We have used the power law index of 3.5 throughout in this paper. However, it may depend on some important physical parameters such as  $\omega_{pe}/\Omega_{ce}$ ,  $\theta_{Bn}$ ,  $m_i/m_e$  etc. We also observe that the spectral index varies with time according to the phase of the self-reformation. The maximum energy of SSA is also important for the electron injection. The maximum energy, which is required in order to account for observations, depends on the shock potential. The maximum energy should be larger than the shock potential to obtain a measurable fraction of reflected electrons. Even in this case, the maximum energy is important for determining the shock angle dependence of the injection efficiency, because it introduces the cut-off shock angle where the injection efficiency rapidly decreases.

We also introduce the escape probability of energetic electrons as another important factor for determining the shock angle dependence. We attribute the probability to the self-reformation of the shock front. This is because the value of the escape probability estimated from the simulation results is  $P_{esc} \simeq 4\Omega_{ci}$ , which indicates that the escape mechanism is, to some extent, related to the shock self-reformation process. Although the self-reformation process of the shock front has been extensively studied by many authors (e.g. Quest 1986; Lembege & Savoini 1992; Scholer et al. 2003), it is still a controversial topic of collisionless shock physics. Shimada & Hoshino (2005) have recently pointed out that the dynamics of the shock front can be modified by strong dissipation due to microinstabilities in the transition region of very high Mach number shocks. Similar phenomenon at moderate Mach number shock  $M_A \sim 6$  is also reported by Scholer & Matsukiyo (2004), where the modified two stream instability plays an important role (e.g. Matsukiyo & Scholer 2003). It is difficult to say whether the shock self-reformation process survives in real SNR shocks, where strong dissipation of both electrons and ions is expected. If the self-reformation is suppressed by strong dissipation, the escape probability may become smaller. If this is the case, the cut-off shock angle determined by the escape probability disappears and the maximum cut-off energy of SSA controls the shock angle dependence.

If the shock self-reformation is suppressed and the maximum energy of SSA becomes

sufficiently large, the reflection of energetic electrons will take place at the shock angle very close to the threshold between subluminal and superluminal shocks. The relativistic effect becomes important for such situations, because both the effective shock velocity  $V_{sh}$  and the required energy for the reflection become relativistic. In this case, since the shock angle is well close to  $90^\circ$ , the shock potential has little influence on the reflection process, i.e., the relativistic effect does not affect the mirror reflection efficiency in the absence of the electrostatic potential. Thus, the present mechanism should work in principle. It is important to investigate whether highly relativistic electrons are generated via SSA or not. Stochastic version of SSA may be important to understand the issue (McClements et al. 2001).

We should also point out that further electron heating and acceleration in the shock transition region may be possible if multidimensional effects are considered. It is well known that many plasma microinstabilities can be excited within the shock transition region (e.g. Wu et al. 1984). For instance, it is easy to expect that the whistler mode waves are excited by temperature anisotropy ( $T_\perp > T_\parallel$ ) of thermal electron because of strong perpendicular heating and acceleration due to SSA and the ion acoustic turbulence. We also expect that the reflected electron beam with temperature anisotropy ( $T_\perp > T_\parallel$ ) will excite the whistler waves propagating antiparallel to the beam by cyclotron resonance as discussed by Tokar et al. (1984), although the use of one-dimensionality assumption in the present simulation inhibits the excitation of these instabilities. If the whistler wave intensity becomes sufficiently strong, both the beam and core electron distributions will become isotropic via strong pitch angle scattering. The first adiabatic invariant of electron will be violated and our simple theoretical model using the adiabatic approximation may be inaccurate. Even in this case, there are no reason why SDA should not operate, because the physical mechanism is quite simple and does not require any special conditions. However, the process will be strongly modified by the turbulence in the shock transition region. The wave-particle interaction within the shock layer may provide further heating and acceleration of electrons. We would like to emphasize again the significant importance of SSA on the energization of electrons. SSA plays a key role in the turbulent shock structure in the sense that it provides additional sources of free energy and may lead to further energization of electrons.

The relation between the electron acceleration efficiency and the whistler waves is recently studied by Oka et al. (2006). They analyzed a number of the Earth's bow shock crossing events observed by Geotail. They clearly showed that the power law index of electron energy spectra measured in the shock transition region is regulated by the so-called whistler critical Mach number  $M_{crit}^w$ , which is defined as the critical point above which the whistler waves cannot propagate upstream. The spectral indices are distributed 3.5 – 5.0 in the sub-critical regime, while the harder energy spectra with indices of 3.0 – 3.5 are observed

in the super-critical regime. In the super-critical regime, the whistler waves generated by microinstabilities are accumulated in the shock transition region. Since SNR shocks are in super-critical regime, we can expect that the accumulated energy of the whistler waves may contribute to further electron energization. It is interesting to investigate the relationship between the whistler waves and the electron acceleration efficiency. Gyroresonant surfing acceleration proposed by Kuramitsu & Krasnoselskikh (2005) might be important.

In order to model such nonadiabatic processes, we must know the shock structure (e.g. shock potential, nonstationarity) and the wave activity in the transition region of realistic high Mach number shocks in more detail. Numerical simulation of self-consistent shock structures including the whistler wave turbulence requires at least two-dimensional simulation domain which demands very large computational resources. Another possibility to improve the understandings of high Mach number shocks is in situ observation of interplanetary shocks in the inner heliosphere. It is known that interplanetary shocks driven by Coronal Mass Ejections (CMEs) can be very high Mach number near the Sun (e.g. Smart & Shea 1985). Expected Mach number at the Mercury orbit of  $\sim 0.4$  AU becomes  $M_A \sim 40$ . Observations of such interplanetary shocks may provide us useful information to understand the physics of electron acceleration at very high Mach number shocks.

In the present paper, we have restricted ourselves to the discussion of the electron injection process. The self-generation of upstream waves is one of the major problems of the electron DSA theory. The cyclotron resonance condition between the reflected electron beam and a left-hand polarized weakly damped Alfvén wave ( $kv_A/\Omega_{ci} \lesssim 1$ ) requires,

$$\frac{v_r}{V_1} \gtrsim \frac{1}{2} \frac{1}{M_A} \frac{m_i}{m_e}, \quad (26)$$

where the factor 1/2 in the right-hand side of the above equation indicates the difference of the frame between the shock frame and the upstream frame. If we use typical Mach number of SNR shocks  $M_A \sim 100 - 1000$ , this condition becomes  $v_r/V_1 \gtrsim 1 - 10$ . By combining (17) and (26), we can estimate the critical Mach number above which the self-generation of upstream waves becomes possible. Figure 9 shows the shock angle dependence of the critical Mach number. We confirm that the self-generation of upstream waves is indeed possible in typical SNR shocks, i.e., our theory successfully explains the electron injection as well as the triggering of subsequent DSA process.

Since we also know the reflected electron density, we can, in principle, estimate the wave intensity, hence, the diffusion coefficient of energetic electrons using quasi-linear theory. However, we think that it is rather important to investigate further electron energization in the shock transition region introduced by multidimensional effect before we discuss the consequence of the electron injection and subsequent DSA process.

Another important problem is the back-reaction from nonthermal particles. It is known that the energetic particles affect the upstream plasma environment when their energy density becomes comparable to that of the background plasma (e.g. Drury & Volk 1981). We cannot discuss such a nonlinear evolution in the present model, because we do not consider the injection process of ions. Obviously, ions have much larger energy density than that of electrons. Thus, the injection efficiency of ions is more important to understand the shock structure in the presence of energetic particles. In order to study the nonlinear evolution including the interaction between thermal and nonthermal particles, the injection efficiencies of both electrons and ions will be of great importance. Understanding of both the injection processes and the nonlinear shock structure will elucidate the problem of cosmic ray acceleration at collisionless shock waves.

This work is supported by ISAS/JAXA and the Solar-Terrestrial Environment Laboratory, Nagoya University. T.A. is supported by JSPS Research Fellowship for Young Scientists.

### A. Calculation of Reflection Time

The parallel equation of motion in the HTF under the action of the magnetic mirror force and the electrostatic potential can be written as

$$m_e \frac{dv_{\parallel}}{dt} = - \left( \mu \frac{\partial B}{\partial x} + e \frac{\partial \phi}{\partial x} \right) \cos \theta_{Bn}, \quad (\text{A1})$$

where  $x$  represents the particle position and  $\mu = m_e v_{\perp}^2 / 2B$  is the first adiabatic invariant. By assuming the spatial gradients of both the magnetic field strength and the electrostatic potential are constant, we can integrate the equation,

$$x(t) = v_{\parallel}(0)t - \frac{\cos \theta_{Bn}}{2m_e} \frac{\mu \Delta B - e \Delta \phi}{\Delta x} t^2. \quad (\text{A2})$$

In this calculation, we have neglected the curvature of the magnetic field line in the shock transition region for simplicity (i.e.  $\cos \theta_{Bn} = \text{const.}$ ). The initial parallel velocity is  $v_{\parallel}(0) \simeq V_{sh}$  and the shock width is approximately given by  $\Delta x \simeq V_1 / \Omega_{ci}$ . Then, we obtain the characteristic time for the reflection process  $T_{ref}$  as

$$\Omega_{ci} T_{ref} \simeq \frac{2m_e V_{sh}^2}{\mu \Delta B - e \Delta \phi}. \quad (\text{A3})$$

If we use the definition of the characteristic particle energy perpendicular to the magnetic field before the reflection  $E_{ref} = m_e v_{\perp}^2 / 2$ ,

$$\begin{aligned} \mu \Delta B &= E_{ref} \frac{B_{\max} - B_f}{B_f} \\ &= \frac{E_{ref}}{\tan^2 \theta_c}. \end{aligned} \tag{A4}$$

Thus, we can rewrite the reflection time

$$\Omega_{ci} T_{ref} \simeq \frac{2m_e V_{sh}^2}{E_{ref} / \tan^2 \theta_c - e \Delta \phi}. \tag{A5}$$

It is easy to understand that  $T_{ref}$  is proportional to  $1 / \cos^2 \theta_{Bn}$  for the fixed particle energy. The reflection time becomes shorter with increasing the particle energy.

## REFERENCES

- Allen, G. E., Petre, R., & Gotthelf, E. V. 2001, *ApJ*, 558, 739
- Anderson, K. A. 1969, *J. Geophys. Res.*, 74, 95
- Anderson, R. R., Eastman, T. E., Gurnett, D. A., Frank, L. A., & Parks, G. K. 1981, *J. Geophys. Res.*, 86, 4493
- Bale, S. D., Hull, A., Larson, D. E., Lin, R. P., Muschietti, L., Kellogg, P. J., Goetz, K., & Monson, S. J. 2002, *ApJ*, 575, L25
- Bale, S. D., Kellogg, P. J., Larson, D. E., Lin, R. P., Goetz, K., & Lepping, R. P. 1998, *Geophys. Res. Lett.*, 25, 2929
- Bamba, A., Yamazaki, R., Ueno, M., & Koyama, K. 2003, *ApJ*, 589, 827
- Bell, A. R. 1978a, *MNRAS*, 182, 147
- . 1978b, *MNRAS*, 182, 443
- Blandford, R. D., & Ostriker, J. P. 1978, *ApJ*, 221, L29
- Buneman, O. 1958, *Phys. Rev. Lett.*, 1, 8
- Cargill, P. J., & Papadopoulos, K. 1988, *ApJ*, 329, L29

- Dieckmann, M. E., Chapman, S. C., McClements, K. G., Dendy, R. O., & Drury, L. O. 2000a, *A&A*, 356, 377
- Dieckmann, M. E., Eliasson, B., Stathopoulos, A., & Ynnerman, A. 2004, *Phys. Rev. Lett.*, 92, 065006
- Dieckmann, M. E., Ljung, P., Ynnerman, A., & McClements, K. G. 2000b, *Phys. Plasmas*, 7, 5171
- Drury, L. O., & Volk, J. H. 1981, *ApJ*, 248, 344
- Eichler, D. 1981, *ApJ*, 244, 711
- Forslund, D. W., Quest, K. B., Brackbill, J. U., & Lee, K. 1984, *J. Geophys. Res.*, 89, 2142
- Gosling, J. T., Asbridge, J. R., Bame, S. J., Feldman, W. C., Zwickl, R. D., Paschmann, G., Sckopke, N., & Hynds, R. J. 1981, *J. Geophys. Res.*, 86, 547
- Hoshino, M. 2001, *Prog. Theor. Phys. Suppl.*, 143, 149
- Hoshino, M., & Shimada, N. 2002, *ApJ*, 572, 880
- Hull, A. J., Larson, D. E., Wilber, M., Scudder, J. D., Mozer, F. S., Russell, C. T., & Bale, S. D. 2006, *Geophys. Res. Lett.*, 33, 15104
- Ishihara, O., Hirose, A., & Langdon, A. B. 1981, *Phys. Fluids*, 24, 452
- Kasaba, Y., Matsumoto, H., Omura, Y., Anderson, R. R., Mukai, T., Saito, Y., Yamamoto, T., & Kokubun, S. 2000, *J. Geophys. Res.*, 105, 79
- Katsouleas, T., & Dawson, J. M. 1983, *Phys. Rev. Lett.*, 51, 392
- Krauss-Varban, D., Burgess, D., & Wu, C. S. 1989, *J. Geophys. Res.*, 94, 15089
- Krauss-Varban, D., & Wu, C. S. 1989, *J. Geophys. Res.*, 94, 15367
- Kuramitsu, Y., & Krasnoselskikh, V. 2005, *Phys. Rev. Lett.*, 94, 031102
- Lee, M. A. 1982, *J. Geophys. Res.*, 87, 5063
- Lee, M. A., Shapiro, V. D., & Sagdeev, R. Z. 1996, *J. Geophys. Res.*, 101, 4777
- Lembege, B., & Savoini, P. 1992, *Phys. Fluids*, 4, 3533
- Leroy, M. M., & Mangeney, A. 1984, *Ann. Geophys.*, 2, 449

- Leroy, M. M., Winske, D., Goodrich, C. C., Wu, C. S., & Papadopoulos, K. 1982, *J. Geophys. Res.*, 87, 5081
- Levinson, A. 1992, *ApJ*, 401, 73
- Long, K. S., Reynolds, S. P., Raymond, J. C., Winkler, P. F., Dyer, K. K., & Petre, R. 2003, *ApJ*, 586, 1162
- Matsukiyo, S., & Scholer, M. 2003, *J. Geophys. Res.*, 108, 19
- McClements, K. G., Dieckmann, M. E., Ynnerman, A., Chapman, S. C., & Dendy, R. O. 2001, *Phys. Rev. Lett.*, 87, 255002
- Oka, M. 2005, PhD Thesis, University of Tokyo
- Oka, M., Terasawa, T., Seki, Y., Fujimoto, M., Kasaba, Y., Kojima, H., Shinohara, I., Matsui, H., Matsumoto, H., Saito, Y., & Mukai, T. 2006, *Geophys. Res. Lett.*, 33, 24104
- Papadopoulos, K. 1988, *Ap&SS*, 144, 535
- Quest, K. B. 1986, *J. Geophys. Res.*, 91, 8805
- Sagdeev, R. Z. 1966, *Rev. Plasma Phys.*, 4, 23
- Schmitz, H., Chapman, S. C., & Dendy, R. O. 2002a, *ApJ*, 579, 327
- . 2002b, *ApJ*, 570, 637
- Scholer, M., Hovestadt, D., Ipavich, F. M., & Gloeckler, G. 1980, *J. Geophys. Res.*, 85, 4602
- Scholer, M., & Matsukiyo, S. 2004, *Ann. Geophys.*, 22, 2345
- Scholer, M., Shinohara, I., & Matsukiyo, S. 2003, *J. Geophys. Res.*, 108, 4
- Shimada, N., & Hoshino, M. 2000, *ApJ*, 543, L67
- . 2005, *J. Geophys. Res.*, 110, 2105
- Shimada, N., Terasawa, T., Hoshino, M., Naito, T., Matsui, H., Koi, T., & Maezawa, K. 1999, *Ap&SS*, 264, 481
- Smart, D. F., & Shea, M. A. 1985, *J. Geophys. Res.*, 90, 183
- Thomsen, M. F., Gosling, J. T., Bame, S. J., Quest, K. B., & Winske, D. 1987, *J. Geophys. Res.*, 92, 2305



- Tokar, R. L., Gurnett, D. A., & Feldman, W. C. 1984, *J. Geophys. Res.*, 89, 105
- Vandas, M. 1995, *J. Geophys. Res.*, 100, 21613
- . 2001, *J. Geophys. Res.*, 106, 1859
- Wu, C. S. 1984, *J. Geophys. Res.*, 89, 8857
- Wu, C. S., Winske, D., Tanaka, M., Papadopoulos, K., Akimoto, K., Goodrich, C. C., Zhou, Y. M., Tsai, S. T., Rodriguez, P., & Lin, C. S. 1984, *Space Sci. Rev.*, 37, 63
- Yamazaki, R., Yoshida, T., Terasawa, T., Bamba, A., & Koyama, K. 2004, *A&A*, 416, 595
- Zank, G. P., Pauls, H. L., Cairns, I. H., & Webb, G. M. 1996, *J. Geophys. Res.*, 101, 457

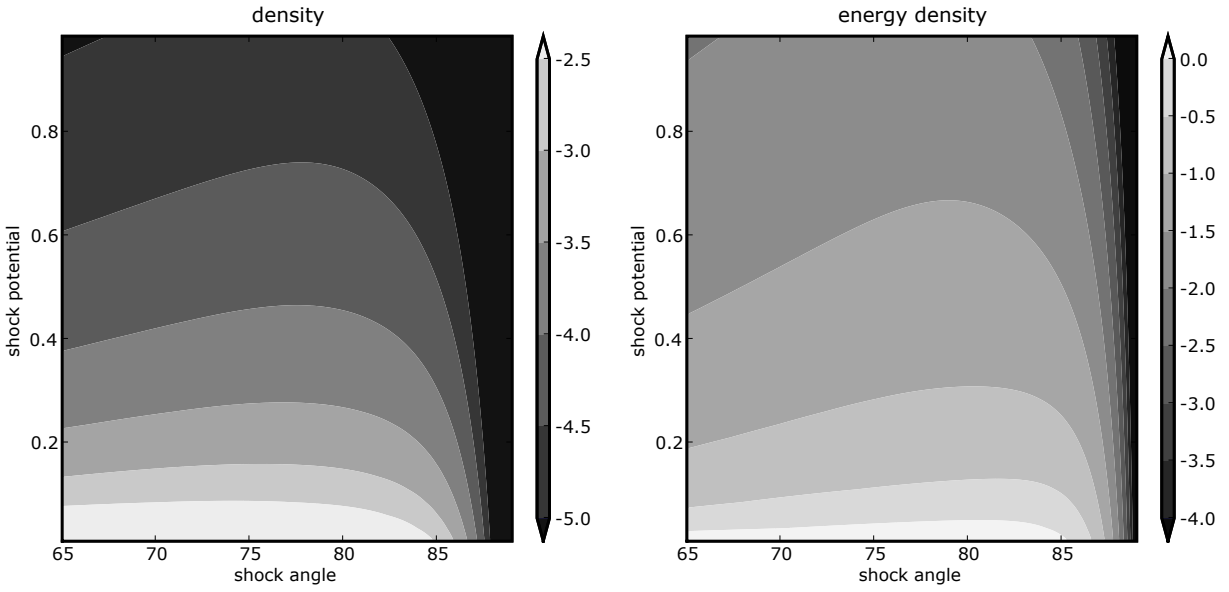


Fig. 8.— Density (left) and energy density (right) of reflected electrons. The contour levels are equally spaced on a logarithmic scale. The vertical axis represents the shock potential normalized to the ion bulk energy in the upstream.

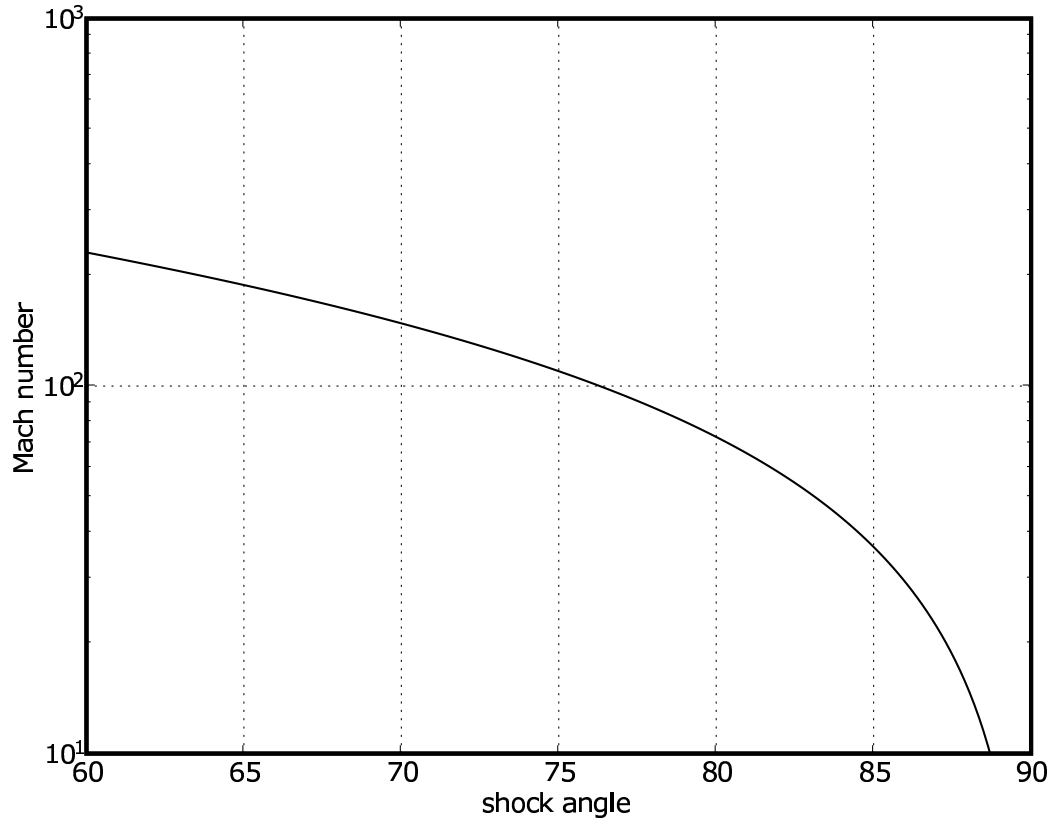


Fig. 9.— Critical Mach number above which the self-generation of upstream waves becomes possible.